# Dalton Transactions

Accepted Manuscript






ROYAL SOCIETY OF CHEMISTRY

www.rsc.org/dalton

Journal Name

ARTICLE

# Flexible MOFs Under Stress: Pressure and Temperature

Abraham Clearfield*

Received 00th January 20xx,
Accepted 00th January 20xx

DOI: 10.1039/x0xx00000x

www.rsc.org/

In the recent past an enormous number of Metal-Organic Framework type compounds (MOFs) have been synthesized. The novelty resides in their extremely high surface area and the ability to include additional features to their structure either during synthesis or as additives to the MOF. This versatility allows for MOFs to be designed for specific applications. However, the question arises as to whether a particular MOF can withstand the stress that may be encountered in fulfillment of the designated application. In this study we describe the behavior of two flexible MOFs under pressure and several others under temperature increase. The pressure study includes both experimental and theoretical calculations. In the thermal processes evidence for colossal negative thermal expansion were encountered.

## 1. Introduction

Metal-organic frameworks, MOFs, have emerged as an extensive class of crystalline materials with ultra high porosity and enormous internal surface areas. These properties together with the extraordinary degree of variability for both the organic and inorganic components of their structures make MOFs of interest for potential applications in clean energy, as storage media for gases such as hydrogen and methane and a high-capacity absorbents to meet various separation needs. Many other applications are under intense investigation. These opening remarks by Jeffrey Long, Omar Yaghi and Hong Cai Joe Zhou [1] Editors of a special issue on MOFs, is a prelude to the enormous diversity and promise of this relatively new area of chemistry. As they further state MOFs epitomize the beauty of chemical structures and the power of combining organic and inorganic chemistry, two disciplines often regarded as disparate.

Our interest in MOFs is to determine their response to temperature and pressure. The compounds we describe here are flexible. A review of such compounds has recently been published covering years 2009-2013[2]. The authors state that these materials can respond to physical and chemical stimuli of various kinds, such as light, mechanical, thermal, electrical or magnetic forces. In this paper we will describe our results of flexible MOFs under pressure and temperature. We shall also provide some insight into our rigid UMOFs.

## 2. MOFs under Pressure

*Department of Chemistry, Texas A&M University, P. O. Box 30012, College Station, TX 77842-3012, USA, E-mail: clearfield@chem.tamu.edu*

The number of MOFs that have been subjected to mechanical stress is small compared to the vast number of MOFs that have been synthesized. One of the earliest studies was by Cheetham and Tan[3]. This paper is in the form of a review with 137 references. In this review the authors emphasized the importance of zeolitic imidazolate frameworks, (ZIFs), as a unique class of MOFs that were subjected to high pressure, by Chapman et al.[4]. They stressed the fact that because of the very high surface areas of MOFs, application of pressure may distort the framework and pore structure which in turn may significantly alter the guest sorption properties. Changes in pore size, In the case of Zn (2-methylimidazole)$_2$(ZIF-8), when subjected to hydrostatic conditions, the framework compresses rapidly, 5% over 0.3 GPa[5]. Further increases in pressure resulted in the sample being amorphizied. However $N_2$ absorption showed that even in this condition the compound is porous.

Figure 1 here

In contrast for $Cu_3$(1,3,5-benzenetricarboxylate)$_2$($H_20$)$_3$(Cu-btc)[4], the powder appeared to be incompressible at low pressure, then compressing rapidly at higher pressure. The powder was held in a diamond anvil cell (DAC). The DAC was closed either with no pressure transmitting fluid or with methanol-ethanol-water (MEW) isopropyl alcohol or Fluorint (FC-70 perfluorotri-N-pentylamine) to mediate hydrostatic sample compression.The results are shown in Figure 1 indicating the change in volume of the lattice as a function of applied pressure. In a third paper by the Chapman group[6] they used activated ZIF-8 to sorb radioactive $I_2$ in increasing quantities. The samples were then amorphizied. The pore apertures were sufficiently distorted as to trap the $I_2$. The pressure required for amorphitization was about the same whether the ZIF-8 contained $I_2$ or not. PDF studies showed that the short range framework order in the amorphous solid was little changed from the long range order of the crystalline ZIF-

8. It is suggested that ZIF-8 might be useful for interim storage or controlled release applications. Moggach, et al. have shown the "effects of" pressure on crystalline porous frameworks and the structural changes associated with forcing solvent into the pores[7,8]. The different types of transformations of MOFs that occur as a result of applying mechanical pressure are illustrated in Figure 2. The pressure structures referenced have been conducted on relatively rigid, highly porous MOFs.

Our interest in MOFs is to determine their response to temperature and pressure. The compounds we describe here are flexible. A review of such compounds has recently been published covering years 2009-2013[2]. The authors state that these materials can respond to physical and chemical stimuli of various kinds, such as light, mechanical, thermal, electrical or magnetic forces. In this paper we will describe our results of flexible MOFs under pressure and temperature. We shall also provide some insight into our rigid UMOFs.

Figure 2 here

## 3. The ZAG MOFs Under Pressure

Our own interests centered on metal phosphonates with both rigid and flexible linkers[9-12]. Among the compounds synthesized were alkyl $C_4H_8$ and $C_6H_{12}$ diphosphonates of Zinc[11]. Our purpose was to determine how a small pore MOF with flexible linkers would respond to pressure. This is in contrast to the earlier compression studies where the MOFs were highly porous and with rigid linkers. The two compounds subjected are termed ZAG-4 and ZAG-6[11]. The title stands for Zinc alkyl-tunnel gate. The formulas of the two compounds are $Zn(HO_3PC_4H_8PO_3H) \cdot 2H_2O$ and $Zn(HO_3PC_6H_{12}PO_3H) \cdot 2H_2O$. The space group for both compounds is C2/c. The unit cell dimensions are respectively a=18.485(3), b=8.2738(15), c=8.2600(15)Å, β=114.46(2)° and 20.388(4), 8.2663(13), and 8.1857(13)Å, β=102.720(13)°. The representative structures of the two compounds viewed down the C-axis at ambient pressure are shown in Figure 3. The Zn ion is bridged to four others through O-P-O group bridges in two directions to form a 1-D chain of eight membered rings down the C-axis as shown in Figure 4. There are two protons on the phosphonic acids as only half the acid protons were displaced. These POH groups form hydrogen bonds with the two water molecules that are between the inorganic chains forming two dimensional sheets. Finally these sheets are bonded together by the $c_4$ or $c_6$ diphosphonate groups[11].

Figure 3 and 4 here

My former student Kevin Gagnon had been reading the papers by the Chapman and Moggach groups. He was particularly interested about the effect of small pressures upon of single crystals with porous frameworks and the structural changes associated with forcing solvent into the pores[8]. He suggested that we subject the ZAG-4 and 6 compounds as single crystals to pressure to determine how they differ from the highly porous MOFs with rigid linkers. I agreed.

This study was carried out at The Advanced Light Source (ALS) at Lawrence Berkeley National Lab (LBNL). Data collection was performed at Beamline 11.3.1. A crystal of ZAG-4 of dimensions 175 x 60 x 40 µm was loaded into a diamond anvil cell (DAC). The pressure medium used was a 4:1 methanol/ethanol mixture. The crystal was first affixed to the surface of the diamond culet using a silicone vacuum grease before the gasket was set in place. A small amount of ruby powder was used for pressure calibration. The cell was pressurized to 1.65 GPa initially and allowed to stabilize for 3 hours before data collection. The in situ diffraction experiments were performed using synchrotron radiation (λ=0.60480 Å) on a modified Bruker APEX—II diffractometer system. Three data sets were run at each pressure with a rotation of the DAC by 120˚ resulting in 3 total data sets per pressure. Data were collected at pressures of 1.65 (10) GPa to 7.32 GPa.

In Figure 5 (right side) the compression of the unit cell and the shift in position of the alkyl chains are illustrated. The change in cell volume as a function of pressure is shown in Figure 6 and the relative change in the cell parameters are provided in Figure 7. Note that the β-angle increases over the entire range of pressure from an initial value of 113.837(2)˚ to 123.227(8)˚.

Figure 5 and 6 here

The a and c-axes decrease with pressure increase while the b-axis decreases and then increases and levels off at a fairly constant value. Some of the largest changes in the structure are located in the inorganic 1-D chain in the c-axis direction. Inspection of the eight membered rings, Figure 8, provides an explanation. This figure shows the 8-membered ring at ambient pressure (A) and at 7.32(7) GPa (B). Note that under pressure the O1-Zn1-O2' angle is increased decreasing the distance between Zn1 to Zn2 from 4.245(1) Å to 3.754(1) Å. The angle O1-Zn1-O2 increases from 109.54(8)˚ to 114.7(3)˚.

Figure 7 and 8 here

We now turn our attention to the changes under pressure of the b-axis. This axis is perpendicular to the c-axis along which the chains of eight member rings lie. It is held together by hydrogen bonds between the included water molecule and the free P-OH groups. The exact positions of the hydrogen atoms in the hydrogen bonds could not be determined but the O-O distances were determined with good results. The shortest hydrogen bond O3-H3-O1W decreased from 2.557(3) to 2.37(2) Å when subjected to pressure. This occurs initially at low pressure increases. The caged water molecules collapse inward to fill the free space. However, the existence of the hydrogen atoms on the caged water molecules reduces the amount of room available and limits the amount of compression. After a pressure of about 2.8 GPa is reached an

increase in the b-lattice parameter is observed (Figure 7). The channel of hydrogen bonds combined with expansion of the lateral direction of the inorganic chain explains the initial decrease followed by an increase and finally very little further change at higher applied pressure. We shall show as a result of computational studies carried out by the Coudert group that more than meets the eye is involved[14].

The two ZAG compounds are isoreticular as shown in Figure 3 and both have a wine rack framework. Both exhibit negative linear compressibility at high pressure. They differ in that ZAG-4 acts as a rigid linker (Figure 5) with only the β-angle increasing. In contrast the longer six carbon chain exhibits a coiling transition under pressure (Figure 9). Despite the very large decreases in volume and changes in the unit cell constants, after raising the pressure to 9.9 GPa and upon rapid removal of the pressure, complete reversibility ensued. The original and final cell parameters as well as the final ambient values after compression are provided in reference 13.

## 4. Theoretical Treatment of the ZAG MOFs Under Pressure

Shortly after our paper appeared[13] Francois-Xavier Coudert indicated an interest in our study and inquired whether his group could carry out a theoretical treatment of our experimental results. Both Kevin and I agreed and what follows are the results of this effort[14]. The calculations were able to confirm that both ZAG-4 and 6 undergo negative linear compressibility (NLC) at high pressure and that this is due to the pressure induced structural transition involving a reversible proton transfer between the water molecule and the linker's phosphonate group. Moreover, while the 4-carbon alkyl chain of ZAG-4 acts as a rigid linker, it is shown that the 6-carbon alkyl chain on ZAG-6 exhibits a coiling transition under pressure. The calculations provide insight into the driving force of the transition. The occurrence of a pressure induced proton transfer is a very rare phenomenon and, ours is the first case ever reported for a metal organic framework.

The quantum mechanical calculations provided a structure in good agreement with the experimental data. However the calculation also could provide accurate positions for the hydrogen atoms which could not be refined from the single crystal data. Initially it was shown that the included water molecule was not protonated and formed three hydrogen bonds with the framework donating two H-bonds to two distinct neighboring phosphonate groups. The calculated HOH-O' distances are given as 1.79 and 1.83 Å. The O-O' distances measured 2.77 and 2.81 Å. A hydrogen bond from the third phosphonate group yielded a POH ··· $OH_2$ distance of 1.46 Å with an O ··· O distance 2.50 Å.

In order to develop a proper theory to explain the negative linear compressibility of the ZAG compounds and the unit cell parameters changes with pressure it was necessary to determine the elastic moduli. This was accomplished by quantum mechanical calculations. These results showed that ZAG-4 has some characteristics of soft porous crystals while being more robust due to its denser structure. It therefore ranks between rigid and soft MOFs. Furthermore ZAG-4 exhibits a single direction of NLC whose value is modest compared to porous wine rack frameworks[8,15]. Moreover, this NLC cannot account for the experimental observation of the NLC at higher pressures which is along a different direction (see b-axis in Figure 7). In the elastic regime the calculations predicted a positive LC for the b-axis. The Coudert group therefore resorted to a series of enthalpy minimization calculations at increasing values of pressure. This methodology can deal with deformation outside the elastic regime to predict structural transitions as demonstrated recently for the MOFs CAU-13 and NOTT-300[16]. Figure 9 compares the results of these calculations relative to the experimental results. The agreement is very good but it also shows a change in slope of the c-axis which was not detected in the experimental data due to the small number of pressures measured. At the same time the b-axis changes direction. These changes are occurring at 3.8 GPa.

Figure 9 here

This shift in direction at 3.8 GPa is attributed to the transfer of a proton from the framework's phosphonate group to the water molecule in between the spaces of the b-axis columns. This situation is depicted in Figure 10 which shows the proximity of the water molecule to the oxygen of the phosphonic acid and on the left the protonated water molecules relative to the chains along the c-axis. At this point it is necessary to understand why pressure stabilizes the coexistence of two charged species $R\text{-}PO^-_3$ + $H_3O^+$ in close proximity. The answer based upon quantum mechanical calculations has to do with the evolution of the O-H distances between the proton and oxygen atom of the water and phosphonate group. The compression brings the $–PO_3H$ group closer to the water molecule as the wine rack pore is compressed. The transfer of the proton forms a short 1.05 Å O-H bond in $H_3O^+$. This results in a smaller distance of the two oxygen atoms, 2.4 Å after the jump vs 2.5 before the proton transfer. The shorter O-O distance allows for a smaller unit cell volume so that the pressure is enough to overcome the initial energy penalty ($P\Delta v > \Delta E$).

Figure 10 here

Additional calculations were carried out to shed more light on the pressure induced proton transfer. For those interested we suggest consulting the original paper[14]. The upshot of this study is that ZAG-4 is a good candidate for a pressure-switchable proton conduction material. This property has been shown to exist in brucite at 11 GPa by single crystal experiments[17] is useful for applications as nanodevices, sensors or actuators. ZAG-4 has the advantage over stiff

inorganic materials such as brucite that the proton transfer occurs at a much lower pressure.

## 5. ZAG-6 Linker Coiling

Our earlier paper[13] did not include the crystal structure data for ZAG-6. This information was presented in the supplementary section in our second paper[14]. I include it here for the convenience of the reader. As can be seen in Figure 3 at ambient conditions ZAG-6 has the same wine rack geometry as ZAG-4. Its pores also contain one water molecule in close proximity of each phosphonate group. At high pressure, 6.9 GPa, again the negative compressibility along the b-axis is observed (2% expansion). However the high pressure structure exhibits a coiling of the hexanediphosphonate chain. For ZAG-4 all the alkyl chain dihedral angles stay equal at 180˚ at all pressures investigated. In contrast the ZAG-6 alkyl chain distorts at 6.9 GPa from 177.1(2)˚ to 170.2(6)˚ for the first three carbon atoms in the alkyl chain and from 173.7(3)˚ to 55.3(10)˚ for the first four carbon atoms in the chain. This pressure induced coiling of a flexible linker chain is novel in flexible MOFs which has never been demonstrated before.

Additional calculations were carried out to confirm that the unprotonated $H_2O$ and the straight alkyl chain is the most stable structure at ambient conditions. Furthermore, the cost of coiling the ZAG-6 chain is 15 KJ/mol per primitive cell or 7.5 KJ/mol per alkyl chain. The proton transfer state is destabilized by 25 KJ/mol the same as for ZAG-4. The calculations further show that the coiled $H_3O^+$ structure is the most stable at pressures higher than 3 GPa. This confirms the experimentally observed coiling and its driving force, as well as the occurrence of a pressure induced proton jump as in ZAG-4. This makes ZAG-6 also a candidate pressure-switchable proton conduction material. It should also be mentioned that in the X-ray experimental results a shortening of the P-O bond distance from 1.562(2) to 1.503(9) Å is observed. This is indicative of the change of the phosphonic acid to a phosphonate and indirect experimental evidence of the pressure-induced proton jump.

## 6. Thermoresponsivity

According to Schneemann et al.[2] thermoresponsive MOFs are those that show a reversible change in their lattice parameters after exposure to a temperature program without alteration of the molecular composition. In this context there is a distinction between two phenomena. The frameworks and pores may either shrink or expand, that is, they may undergo negative thermal expansion (NTE) or positive thermal expansion (PTE). Some examples with MOFs are the IRMOFs, described as among the most contracting materials known[18]. Many studies are still being carried out investigating this phenomenon for MOF-5 and HKUST-1[8,19-22]. Non-traditional inorganic metal phosphonates synthesized using the ligand 1,3,5 benzene-triphosphonic acid (BTP) have been investigated for their proton conducting properties[23]. A layered material PCMOF-3 with an extended microstructure of water molecules was synthesized using Zn(II) ions and BTP. This compound provided modest conductivity data due to constrained intergrain proton transfer[23]. An anionic form was also prepared using large cations[24]. However, BTP combined with Cu(II) formed a three dimensional framework where water molecules protrude into the pores leading to a promising proton conductor[25]. To extend PCMOF-3 to a 3D structure a topotactic pillaring approach of anionic layers was used[26,27]. This resulted in four semicrystalline versions of the extended PCMOF-3. One of our studies resulted in the preparation of two anionic 3D frameworks based on Zn-BTP compounds with small amines as countercations[28]. Our approach differed from the pillaring method in that the amines resulted from addition of urea for compound 1 and 1,3-dimethylurea for compound 2 in the hydrothermal procedures. Several sources of protons are present within the pores (ammonium ions, acid protons and water). The formulas are designated as follows: Compound 1, $Zn_{2.5}(H)_{0.4\text{-}0.5}(C_6H_3P_3O_9)(H_2O)_{1.9\text{-}2}(NH_3)_{0.5\text{-}0.6}$. The ammonia arises from decomposition of the urea. Compound 2: $Zn_{2.5}(H)_{0.75}(C_6H_3P_3O_9)(H_2O)_2(CH_3NH_3)_{0.2}$. Our studies showed that the compounds shrink upon heating, reducing the free volume of the pores, thus altering the positions of the solvent molecules. This negative expansion (NTE) is the result of a phase change with some loss of water.

## 7. Crystallographic Studies

Structure determinations of the two zinc compounds were obtained from single crystals on a Bruker-AXS Apex II CCD diffractometer (MoKα, λ=0.71073 Å). Crystallographic parameters and details are provided in Table 2[29]. The ZnBP-$NH_4$ MOF crystallized in the orthorhombic Ibam space group. The asymmetric unit consists of two Zn(II) ions, a BTP molecule situated on a center of symmetry with one-half of the molecule as the asymmetric portion. A water molecule and an ammonium ion complete the half cell. The structure of ZnBP-$NH_4$ consists of a 3D framework built from layers linked by $ZnO_4$ tetrahedra (Figure 11). The $ZnO_4$ centers act as pillars that link an inorganic-organic layer together. The layer is built up from Zn(II) ions in tetrahedral coordination linking columns of BTP molecules. The columns are formed from roughly parallel π- stacked dimers of BTP molecules along the a-axis. In the π stacked dimers the BTP molecules are rotated 180˚ to each other with a π-π distance of 3.672 Å. For each BTP molecule one phosphonate group (P2) lies parallel to the layer and the others (P1) are rotated 60˚ into the interlayer. Within the interlayer, the phosphonate oxygen atoms from a BTP molecule coordinate to eight $ZnO_4$ centers (Zn1-O = 1.905-2.006 Å). The phosphorus oxygen atoms, O2, does not coordinate the interlayer $ZnO_4$ centers. The $ZnO_4$ center, situated above the layer, only coordinates to the oxygen atom O2, from four symmetry equivalent BTP groups (Zn2-

O2=1.930(3) Å). The Zn2 sites act as pillars linking the inorganic-organic layers. This interlayer distance is 9.908 Å, corresponding to half the c-axis.

Figure 11 and 12 here

The 3D framework forms two types of pores that interconnect (Figures 11 and 12). The pores are formed from the spaces between the $ZnO_4$ pillars. The larger pore runs along the [100] direction and the smaller pores run along the [110] direction and interconnect the larger pores. Both pore types are filled with water and ammonium ions. The ammonium ions compensate the -1 charge on the ZnBP framework. The $NH^+_4$/ZnBP ratio is less than one which requires the framework to be partially protonated for charge balance. A topotactic pillaring approach yielded the same compound but only as a powder[26].

**Crystal Structure of ZnBP-$CH_3NH_3$[28,29]** The ZnBP-$CH_3NH_3$ MOF crystallized in the orthorhombic Ibam space group (Table 2). The asymmetric unit consists of two Zn(II) ions, a BTP molecule situated on a center of symmetry with one-half of the molecule as the asymmetric portion, plus a water molecule and a methyl ammonium ion. The framework is isostructural to the ZnBTP framework as shown in Figure 13. The 1, 3-dimethylurea decomposed into methyl ammonium ions. The carbon and nitrogen ions of the methylammonium ions are positionally disordered and occupy two symmetry equivalent sites of the $NH_4^+$ ion in the ZnBP-$NH_4^+$ MOF. The details of the structure are provided in Table 2 right hand column. A figure of the framework is shown in Figure 13.

Figure 13 here

Compound 1 upon heating to 45 °C underwent a phase change (phase II) without loss of solvent: Further heating to 120 °C resulted in a second phase change with loss of solvent (phase III). Rehydration occurs upon exposure to water vapor at 25 °C resulting in return to the initial compound. The structures of the different phases were determined from powder X-ray diffraction data and are provided in Table 3. The crystallographic parameters are similar for all three phases in that the framework remains the same up to 200 °C. Each phase crystallized in the orthorhombic space group Ibam. For phase II at 60 °C, no loss of solvent occurs. The reversible solid-solid transition between phase I and phase II leads to enantiotropic polymorphs. The second solid-solid transition occurs at ~125 °C, which is close to the observed water loss temperature on the TGA curve. The structure of phase III was determined at 150 °C. While the water was lost, the ammonium ions were not, but resided in the larger pores. The change in the free space of the crystal structure is reflected in the change in the unit cell parameters and volume as shown in Figure 14. A negative expansion is exhibited by the compounds as seen by a decrease in volume with an increase in temperature due to dehydration. All cell parameters decrease with an increase in temperature except for the b-axis. The c-axis has the smallest change with a slight decrease that shortens the distance between the layers, narrowing the larger pores. Axis b lies parallel to the layers and is lengthened upon heating, elongating the larger pores. The a-axis decreases the distance between the dimers that in turn decreases the distance between pillars (d- …d distance = 8.443 and 8.296 Å, π…π = 3.720 and 3.669 Å, for phases II and III, respectively). This reduces the size of the smaller pores and no solvent molecules occupy this position.

Figure 14 here

## 8. Microporous Aluminum Phosphonates

The same ligand 1,4-phenyldiphosphonic acid ($H_2O_3PC_6H_4PO_3H_2$) was used to prepare three different compounds by changing the conditions of preparation[30]. The compounds are respectively (1) Al($H_2O$) ($O_3PC_6H_4PO_3H$); (2) $Al_4(H_2O)_2(O_3PC_6H_4PO_3)_3$; (3) $Al_4(H_2O)_4(O_3PC_6H_4PO_3)_{2.84}(OH)_{0.64}$. These compounds, all three undergo reversible dehydration accompanied by structural changes upon being heated. The crystal structures of compounds 1 and 2 were determined using their X-ray powder data. The structure of compound 3 was not determined. High resolution synchrotron data was obtained at the Argonne National Laboratory as described for the zinc compounds.

The structure of compound 1 is illustrated in Figure 15. The structure can be visualized as layered in which the layers are built from $AlO_6$ octahedra bridged together by O-P-O groups to form 8 and 16 member rings (Figure 15, right hand side). These layers form the bc planes and are bridged by the phenyldiphosphonic acid groups into a 3D structure (Figure 15, left side). One proton remains on the phosphonate group for charge balance. Five of the oxygen atoms forming the $AlO_6$ octahedra are derived from five different phosphonate moieties. The sixth oxygen is from a water molecule. The free space in the 16 member rings is occupied by two symmetry dependent water molecules. Upon heating to 180 °C, compound 1 losses its water forming compound 1d which is stable to 440 °C.

Figure 15 here

Upon dehydration of compound 1, the framework is retained but the composition of 1d is Al($O_3PC_6H_4PO_3H$) and the new structure is illustrated in the original paper[30]. The major change is the loss of a water oxygen that was part of the aluminum octahedron. This loss results in formation of aluminum trigonal bipyramidal groups which requires a rearrangement of the inorganic framework. Interestingly, if the Al had chosen a square pyramidal geometry, no change in the framework would have been required. As the geometry transforms from octahedral to trigonal pyramidal the b-axis is shortened from 9.223 to 8.764 Å and the free space in the 8-

and 16- membered rings is decreased. The net result is a decrease in both the a and b-axes and a decrease in volume of the unit cell amounting to 62 $Å^3$. The interlayer distance change is small from 7.296 to 7.266 Å

**Compounds 2 and 2d[30]:** Compound 2 crystallized in space group C2/m (monoclinic) and the asymmetric unit consists of two Al(III) ions, one and a half diphosphonate ions and one water molecule. The aluminium species, $AlO_4$ and $AlO_6$ are coordinated by four or five distinct oxygen phosphonate atoms, respectively, with the $AlO_6$ group bonded to a water oxygen atom. The inorganic layer in the b,c plane is built from double metal chains bridged in the [001] direction forming 12-membered rings (Figure 16, right). Note that starting at the far right are chains built from columns of $AlO_6$ octahedra. Adjacent on the left are chains built from $AlO_4$ tetrahedra running in the direction along the b-axis. These columns are connected to each other with formation of 12-membered rings. These inorganic layers are bridged by two distinct alternating pillared layers in the [100] direction. The first pillared layer is a traditional one in which the pillars (the phenyldiphosphonic acids) are spaced close together to form a densely packed structure. The second pillared layer has the pillars placed apart at every other positon such that channels are formed. The water molecule coordinated to the $AlO_6$ can be seen to protrude into the interlayer spacing of these channels (Figure 16, left). On the basis of elemental analysis and TGA (10.4 wt % $H_2O$) the formula of compound 2 is better represented as $Al_4(H_2O)_2(O_3PC_6H_4PO_3)_3(H_2O)_4$.

Figure 16 here

Upon dehydration of compound 2 between 180 – 200 °C, the composition is converted to $Al_4(O_3PC_6H_4PO_3)_3$. The octahedral aluminium atoms are now five coordinate and the space group reduced to triclinic $P\bar{1}$ as shown in Figure 17 and Table 4. The aluminum atoms form a distorted square pyramidal geometry with a somewhat wider channel. This allows for easier uptake of water. In fact exposure to air results in a rapid recovery to compound 2. This behavior is in contrast to that of compound 1d which remained fixed when exposed to air. Refluxing in water overnight or exposure to the atmosphere for several months is required to regenerate compound 1.

For compound 3 the X-ray powder pattern was not sufficiently developed to obtain the structure. However it did loose water with structure change and rapidly regain water in air similar to compound 2. It is also of interest that the compound $Al_2(OH)_2(H_2O)_2(O_3PCH_2CH_2PO_3)$ dehydrates and rehydrates in a fashion similar to that of compound 2[31].

## 9. UMOFs, Defects and Colossal Negative Thermal Expansion

It has recently been shown that a number of metal organic frameworks contain a certain degree of defects. For example, as pointed out by Cairns and Goodwin[32] zeolitic imidazolate frameworks (ZIFs) On heating to temperatures of 300 °C, a number of ZIF polymorphs undergo framework collapse but do not change their composition[33]. The heated compound is usually amorphous but reheating to 400 °C crystalizes the compound.

An interesting case in which true defects were observed is the case of the MOF Hf-UiO-66[34]. In this study high-resolution synchrotron radiation X-ray powder diffraction combined with Hf L3-edge extended X-ray absorption fine structure was utilized to determine the structure. It essentially has the same structure as Zr-UiO-66. However, this high resolution study revealed the presence of several broadened peaks indicative of structural changes. The powder pattern changes above 100 °C which results in a reduction in the unit cell edge length of the a-axis. At 300 °C the a-axis increased slightly but is further reduced at 400 °C. This was evidence for negative thermal expansion. The reason for doing this study with hafnium in place of zirconium was its potential for the storage of radioactive waste. Hf has a high neutron absorption cross section. What led me to this paper is that my group has been very active in nuclear waste remediation studies for many years[35].

Subsequently the study of defects in the UiO-66 (Hf) system was taken up by Andrew Goodwin and associates[36,37]. Non-stoichiometry had also been reported for the Zr-UiO-66 MOF[38,39] TGA data suggested that one in twelve of the terephthalate groups was missing[36] which was confirmed by neutron scattering[37]. However, the extensive studies by the Goodwin group found that vacancies in UiO-66 (Hf) proceeds in a correlated manner, the position of one vacancy affects the likelihood of vacancies at neighboring sites[36]. A second finding was that vacancies of both the metal cluster and linker sites is possible. These findings may explain many of the difficulties in behavior of these MOFs[36].

Subsequently, a series of UiO-66 MOFs were prepared with increasing amounts of defects. These materials were subjected to thermal treatment so as to assess the framework geometry as a function of temperature[37]. Three primary stages of mass loss were observed, volatilization of fluids at 100 °C, ligand elimination at 250-350 °C and destruction of the framework at 550-600 °C. This elimination results in densification of the framework resulting in isotropic NTE behavior that is many times stronger than that of any other MOF.

Our concern is with a group of materials that we have designated as UMOFs. They are compounds of 4+ ions such as tin and zirconium bonded to organic diphosphonic acids that form porous structures with surface areas of 300-500 $m^2/g$. However, they differ from MOFs in that they are not crystalline as evidenced by a typical X-ray pattern shown as Figure 17.

For this reason we have referred to these compounds as unconventional MOFs (UMOFs). One of their interesting properties is that a second ligand can be inserted so as to prepare compounds such as $Zr(O_3PC_6H_4PO_3)_{1-x/2}(HPO_4)x$. Any number of phosphates and phosphonic acids may be utilized as the second ligand. The particles are nano-structured from 30 to ~100 nm[41]. We view these compounds as highly disordered. Their present utility is that they behave as ion exchangers that prefer ions of high charge (3+, 4+) in preference to ions of lower charge. We are therefore utilizing them to separate lanthanides from actinides[42,43] by oxidizing the actinides to the level 5 oxidation state to form actinyl ions $AcO_2^{+1}$.

Figure 17 here

In attempting to obtain structural information we encounter problems similar to those described for Hf-UiO-66. For example the TGA shows a weight loss of ~12% loss to 115 $^{o}$C, an additional 3-4% to 450-500 $^{o}$C and complete destruction from 500 to 750 $^{o}$C. Also the TGA calculated formula weight is always lower than the molecular weight dictated from the analytical data. It is possible that these UMOFs represent the ultimate defect materials which provides near total disorder, yet functions in a somewhat ordered manner given their preference for high charged ions.

## Acknowledgements

The author thankfully acknowledges his former graduate students Kevin J. Gagnon and Tiffany L. Kinnibrugh. It is they who largely conceived of the ideas for this study and executed the work at the Advanced Light source (K. J. G.) supported by the Office of Science, Office of Basic Energy Sciences of the U.S. Department of Energy and The Advanced Photon Source at Argonne National Laboratory (T. L. K.), supported by the U.S. Department of Energy, Office of Science, Office of Basic Energy Sciences. I owe further thanks to Prof. Francois-Xavier Coudert and his associates for carrying out the theoretical study of the MOF under compression which added so much knowledge to the experimental work. Finally, I am indebted with much thanks to the Robert A. Welch Foundation for the many years that they have supported our work.

## References

1 J. R. Long, O. M. Yaghi, H.-C. Zhou, Editors, *Chem. Review*, 2012, **112**, 673-674.
2 A. Schneemann, V. Bon, I. Schwedler, S. Senkovska, S. Kaskel, R. A. Fischer, *Chem. Soc. Review* 2014, **43**, 6062-6096.
3 J. C. Tan, A. K. Cheetham, *Chem. Soc. Rev.*, 2011, **40**, 1059-1080.
4 K. W. Chapman, G. J. Halder, P. J. Chupas, *J. Am. Chem. Soc.*, 2009, **131**, 17546-17547.
5 K. W. Chapman, G. J. Halder, P. J. Chupas, *J. Am. Chem. Soc.*, 2008, **130**, 10524-10526.
6 K. W. Chapman, D. F. Sava, G. J. Halder, P. J. Chupas, T. M. Nenoff, *J. Am. Chem. Soc.*, 2011, **133**, 18583-18585.
7 A. J. Graham, D. R. Allan, A. Muszkiewicz, C. A. Morrison, S. A. Moggach, *Angew. Chem. Int. Ed.*, 2011, **50**, 11138-11141.
8 J. M. Ogborn, I. E. Collings, S. A. Moggach, A. L. Thompson, A. L. Goodwin, *Chem. Sci.*, 2012, **3**, 3011-3017.
9 S. Konar, J. Zon, A. V. Prosvirin, K. R. Dunbar, A. Clearfield, *Inorg. Chem*., 2007, **46**, 5229-5236.
10 K. J. Gagnon, A. V. Prosvirin, K. R. Dunbar, S. J. Teat, A. Clearfield, *Dalton Trans.*, 2012, **41**, 3995-4006.
11 K. J. Gagnon, S. J. Teat, Z. J. Beal, A. M. Embry, M. E. Strayer, A. Clearfield, *Cryst. Growth and Des.*, 2014, **14**, 3612-3622.
12 K. J. Gagnon, H. P. Perry, A. Clearfield, *Chem Review*, 2011, **112**, 1034-1054.
13 K. J. Gagnon, C. M. Beavers, A. Clearfield, *J. Am. Chem. Soc.*, 2013, **135**, 1252-1255.
14 A. U. Ortiz, A. Boutin, K. J. Gagnon, A. Clearfield, F.-X. Coudert, *J. Am. Chem. Soc.*, 2014, **136**, 11540-11545.
15 A. U. Ortiz, A. Boutin, A. H. Fuchs, F.-X. Coudert, *J. Chem. Phys*., 2013, **138**, 174703.
16 A. U. Ortiz, A. Boutin, F.-X. Coudert, *Chem. Commun.*, 2014, **50**, 5867-5870.
17 X. Guo, T. Yoshino, *Geophys. Res. Lett.*, 2014, **41**, 813-819.
18 D. Dubbeldam, K. S. Walton, D. E. Ellis, *Agnew. Chem. Int. Ed.*, 2007, **46**, 4496-4499
19 N. Lock, M. Christensen, Y. Wu, V. K. Peterson, M. K. Thomsen, R. O. Piltz, A. J. Ramierz-Cuesta, G. J. McIntyre, K. Noren, R. Kutteh, C. J. Kepert, G. J. Kearley, B. B. Iversen, B. B. *Dalton Trans.*, 2013, **42**, 1996-2007.
20 N. Lock, M. Christensen, C. J. Kepert, B. B. Iversen, *Chem. Commun.*, 2013, **49**, 789-791.
21 B. Mu, K. S. Walton, *J. Phys. Chem. C*, 2011, **115**, 22748-22754.
22 W. Zhou, H. Wu, T. Yildirim, J. R. Simpson, W. A. R. Hight, *Phys. Rev. B: Condens. Matter Mater. Phys.*, 2008, **78**, 054114/1.
23 J. M. Taylor, R. K. Mah, I. L. Moudrakovski, C. I. Ratcliffe, R. Vaidhyanathan, G. K. H. Shimizu, *J. Am. Chem. Soc.*, 2010, **132**, 14055.
24 T. Araki, A. Kondo, K. Maeda, *Chem. Commun.*, 2013, **49**, 552-554.
25 D. Kong, J. Zon, J. McBee, A. Clearfield, *Inorg. Chem.*, 2006, **45**, 977-986.
26 K. Maeda, R. Takamatsu, M. Mochizuki, K. Kawawa, A. Kondo, *Dalton Trans.*, 2013, **42**, 10424-10432.
27 H. Maeda, Y. Nishimura, S. Hiroto, H. Shinokubo, *Dalton Trans.*, 2013, **42**, 15885-15888.
28 T. L. Kinnibrugh, A. A. Ayi, V. I. Bakhmutov, J. Zon, A. Clearfield, *Cryst. Growth Des.*, 2013, **13**, 2973-2981.
29 Crystallographic Data from reference 28, compounds obtained in Supplementary data S2, of ref. 28.
30 T. L. Kinnibrugh, V. I. Bakhmutov, A. Clearfield, *Cryst. Growth Des.*, 2014, **14**, 4976-4984.
31 R. N. Devi, P. Wormald, P. A. Cox, P. A. Wright, *Chem. Mater.,* 2004, **16**, 2229-2237.
32 A. B. Cairns, A. L. Goodwin, *Chem. Soc. Rev.* 2013, **42**, 4881-4893.
33 T. D. Bennett, D. A. Keen, J.-C. Tan, E. R. Barney, A. L. Goodwin, A. K. Cheetham, *Angew. Chem. Int. Ed.,* 2011, **50**, 3067-3071.
34 S. Jakobsen, D. Gianolia, D. S. Wragg, M. H. Nilson, H. Emerich, S. Bordiga, C. Lamberti, U. Olsbye, M. Tilset, K. P. Lillerud, *Phys. Rev. B **86***, 125429, (2012).
35 A. Clearfield, *Environmental Application of Nanomaterials - Synthesis, Sorbents and Sensors* 2nd edition, Fryxell, G. E.; Cao, G.; Eds.: Imperial College Press, London, UK. Chapter 7, 159-206 (2012).
36 M. J. Cliffe, W. Wan, X.-O. Zou, P. A. Chater, A. K. Kleppe, M. G. Tucker, H. Wilhelm, N. P. Funnell, F.-X. Coudert, A. L. Goodwin, *Nature Commun.*, 2014, **5**, 4176.

37 M. J. Cliffe, J. A. Hill, C. A. Murray, F.-X. Coudert, A. L. Goodwin, *Phys. Chem. Chem. Phys.* 2015, **17**, 11586-11592.
38 L. Valenzano, B. Civalleri, S. Bordiga, M. Nilsen, S. Jakobsen, K. P. Lillerud, C. Lamberti, *Chem. Mater.*, 2011, **23**, 1700-1718.
39 H. Wu, Y. S. Chua, V. Krungleviciute, M. Tyagi, P. Chen, T. Yildirim, W. Zhou, *J. Am. Chem. Soc.*, **2013, *135***, 10525–10532.
40 A. Clearfield, *Dalton Trans.*, 2008, 6089-6102.
41 K. J. Gagnon, H. P. Perry, A. Clearfield, *Chem. Rev.*, 2012, **112**, 1034–1054.
42 J. D. Burns, T. C. Shehee, A. Clearfield, D. T. Hobbs, *Analytical Chemistry*, (2012), **84**, 6930-6932.
43 J. D. Burns, M. Borkowski, A. Clearfield, D. T. Reed, *Radiochim. Acta*, (2012), **100**, 901–906.

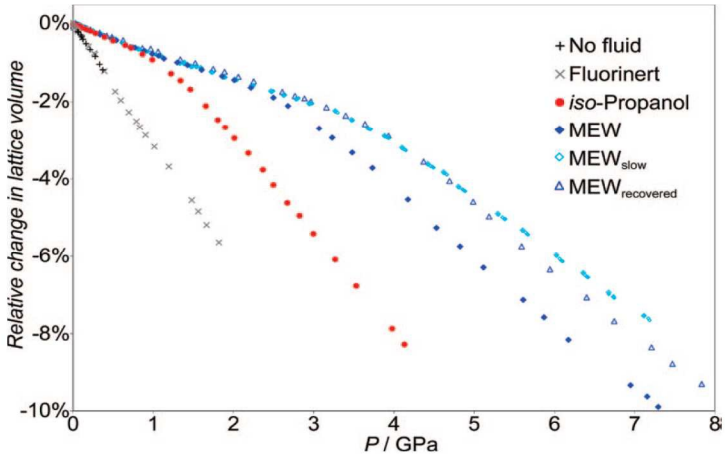


Figure 1. The pressure-induced changes in lattice volume for the **Cu-btc** framework. Errors are within the size of the data points. (Used with permission from J. Am. Chem. Soc. Communications Ref.5)

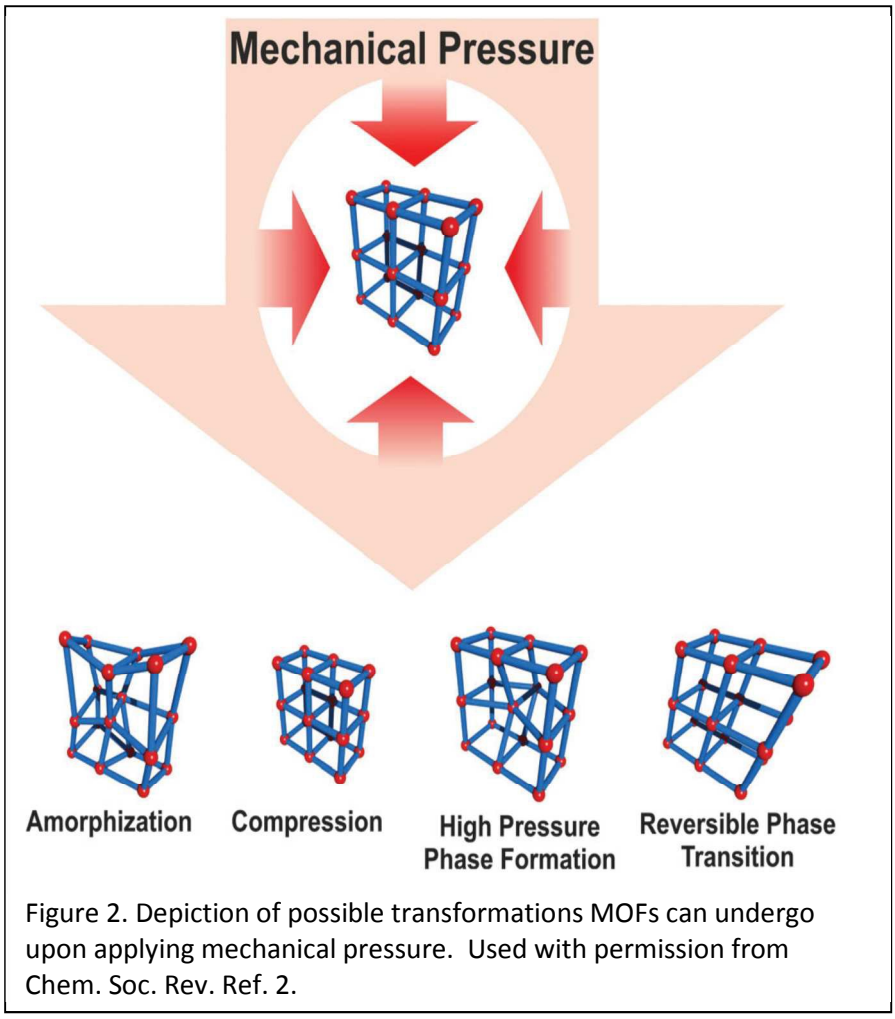


Figure 2. Depiction of possible transformations MOFs can undergo upon applying mechanical pressure. Used with permission from Chem. Soc. Rev. Ref. 2.

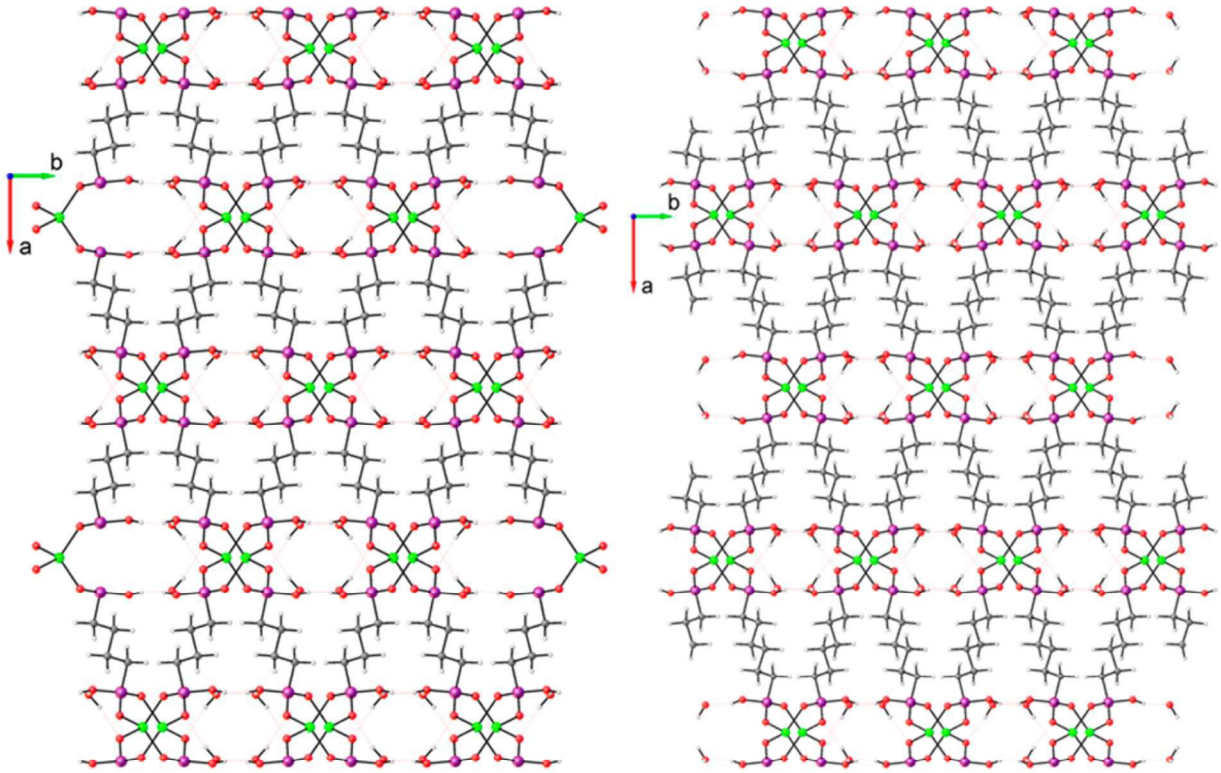


Figure 3. Side-by-side comparison of ZAG-4 (left) and ZAG-6 (right) viewed down the c axis.

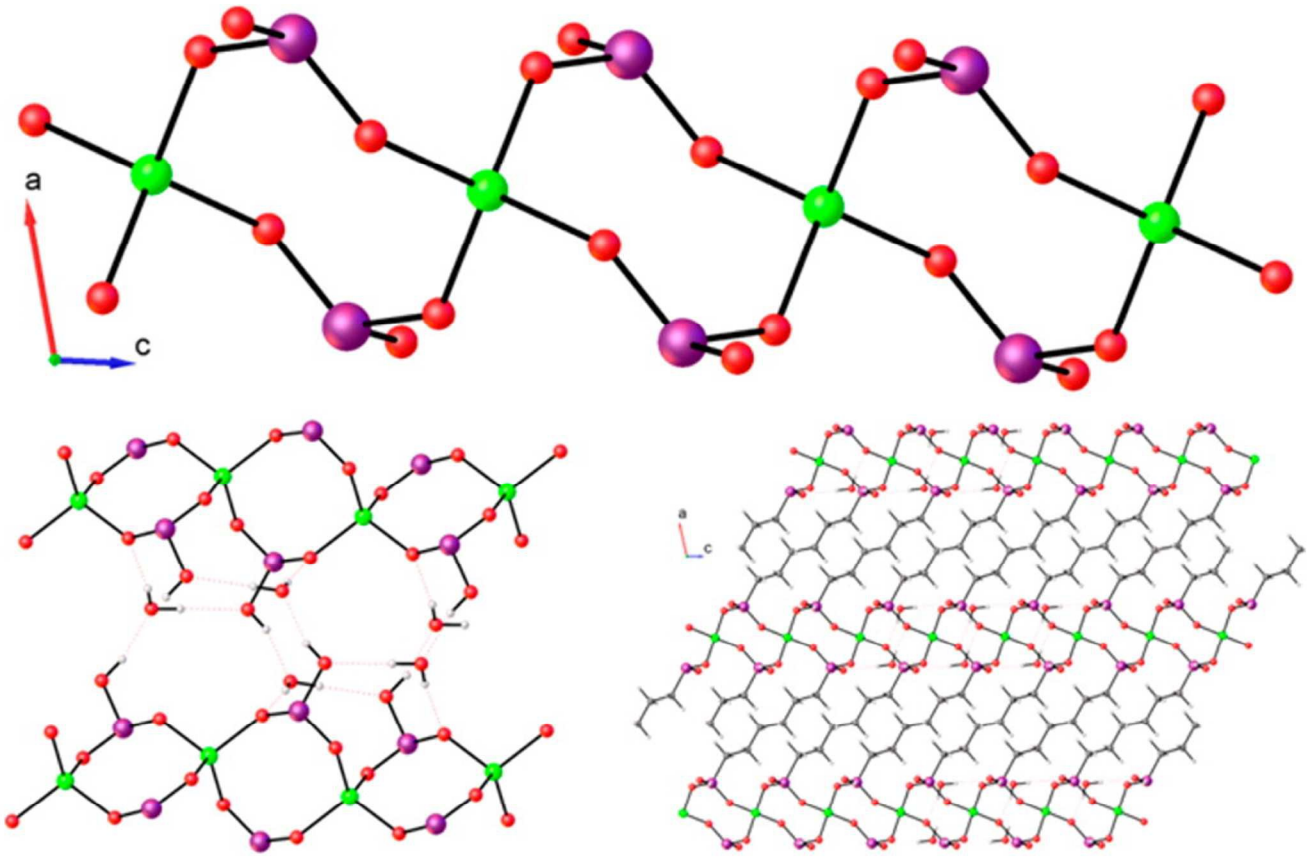


Figure 4. Corner-shared 8-membered Zn-O-P-O rings that make up the 1-D inorganic chain unit of ZAG-6 (top). Localized hydrogen-bonding scheme of ZAG-6 showing the interconnection between 1-D chains via the interstitial water molecules (bottom left). ZAG-6 viewed along the *b* axis showing the cross-linking of the 1-D chains to form the 3-D network (bottom right).

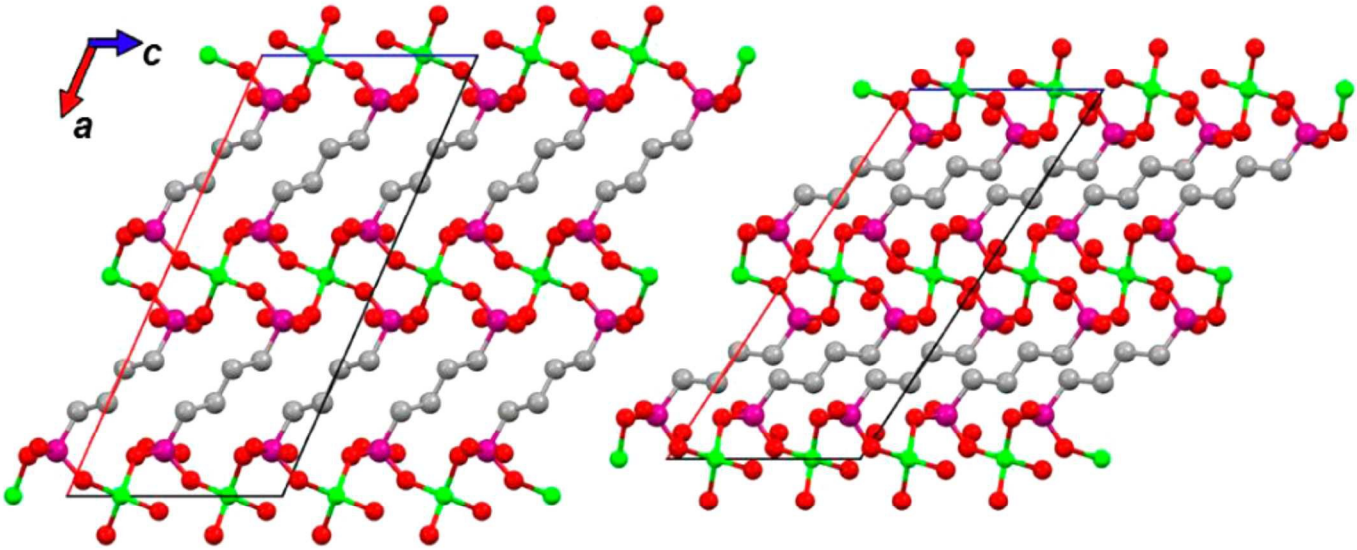


Figure 5. Left side shows the eight membered rings running down the c-axis direction in ZAG-4. These chains are bonded together by the alkyl phosphonate groups. The right side shows same view down the b-axis under a pressure of 7.32(7) GPa. Reproduced from ref. 13 with permission of *J. Amer. Chem. Soc.*

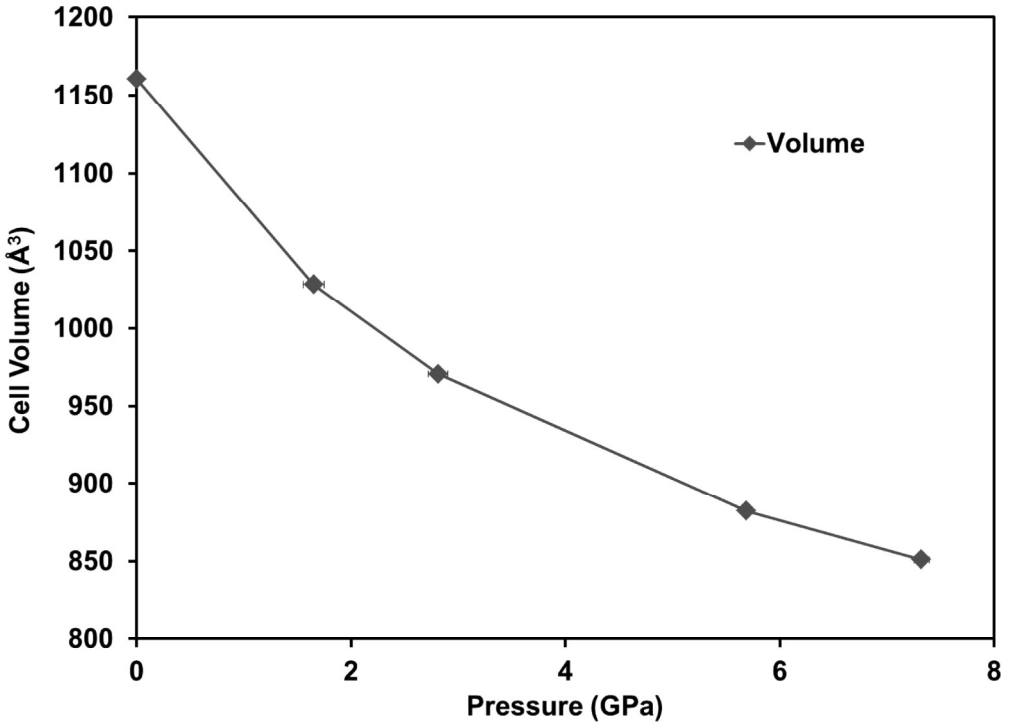


Figure 6. Experimental unit-cell volume variation observed with respect to increase in pressure. This is best fit by a fourth-order Birch−Murnaghan equation of state with K0 = 11.66, K′ = 1.976, and K″ = 1.3776. Vertical error bars are contained within the markers. Taken from reference 13 by permission of *J. Am. Chem. Soc.*

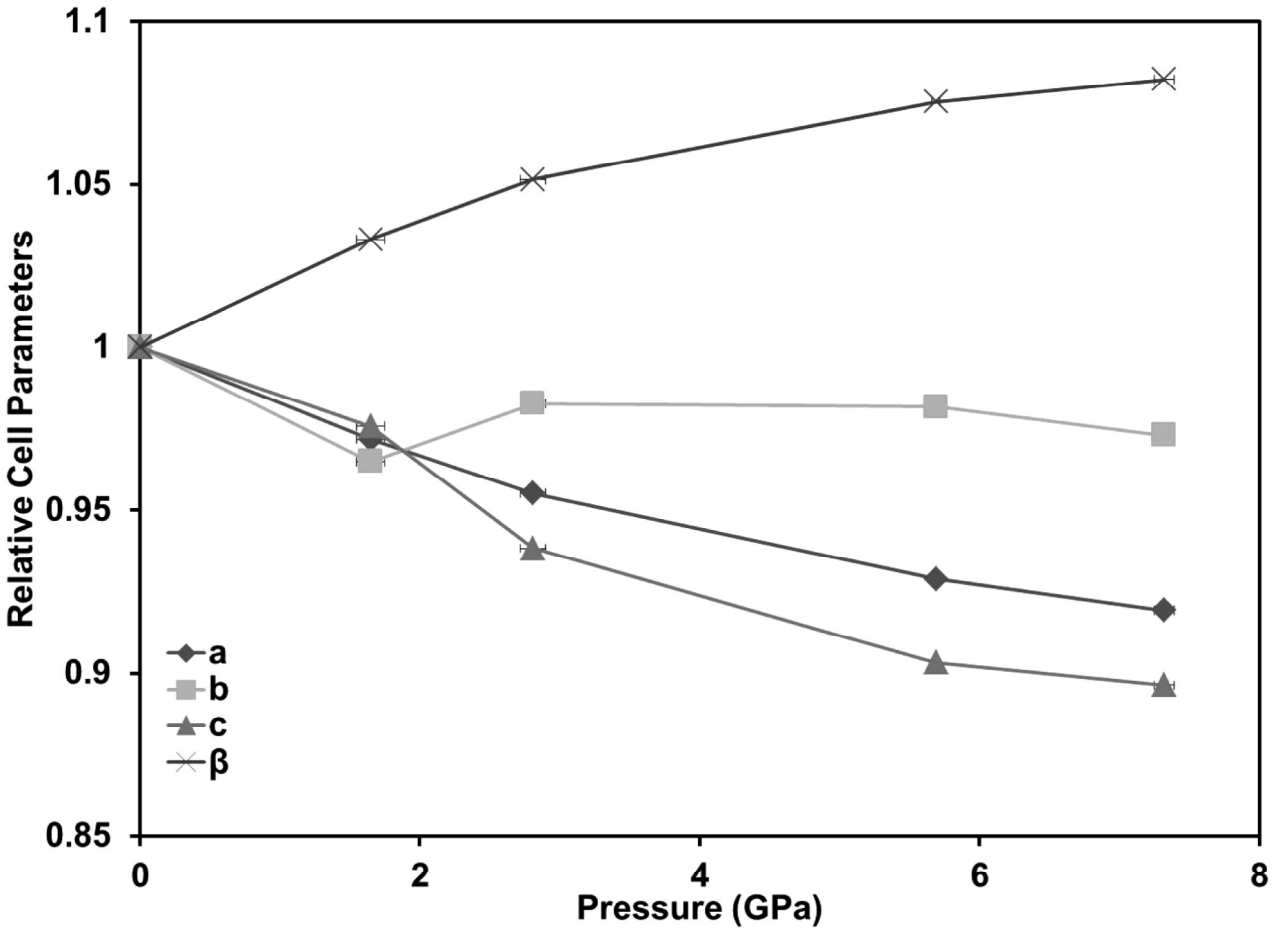


Figure 7. Experimental lattice parameter variation observed with respect to increase in pressure. Vertical error bars are contained within the markers. Taken from reference 13 by permission of *J. Am. Chem. Soc.*

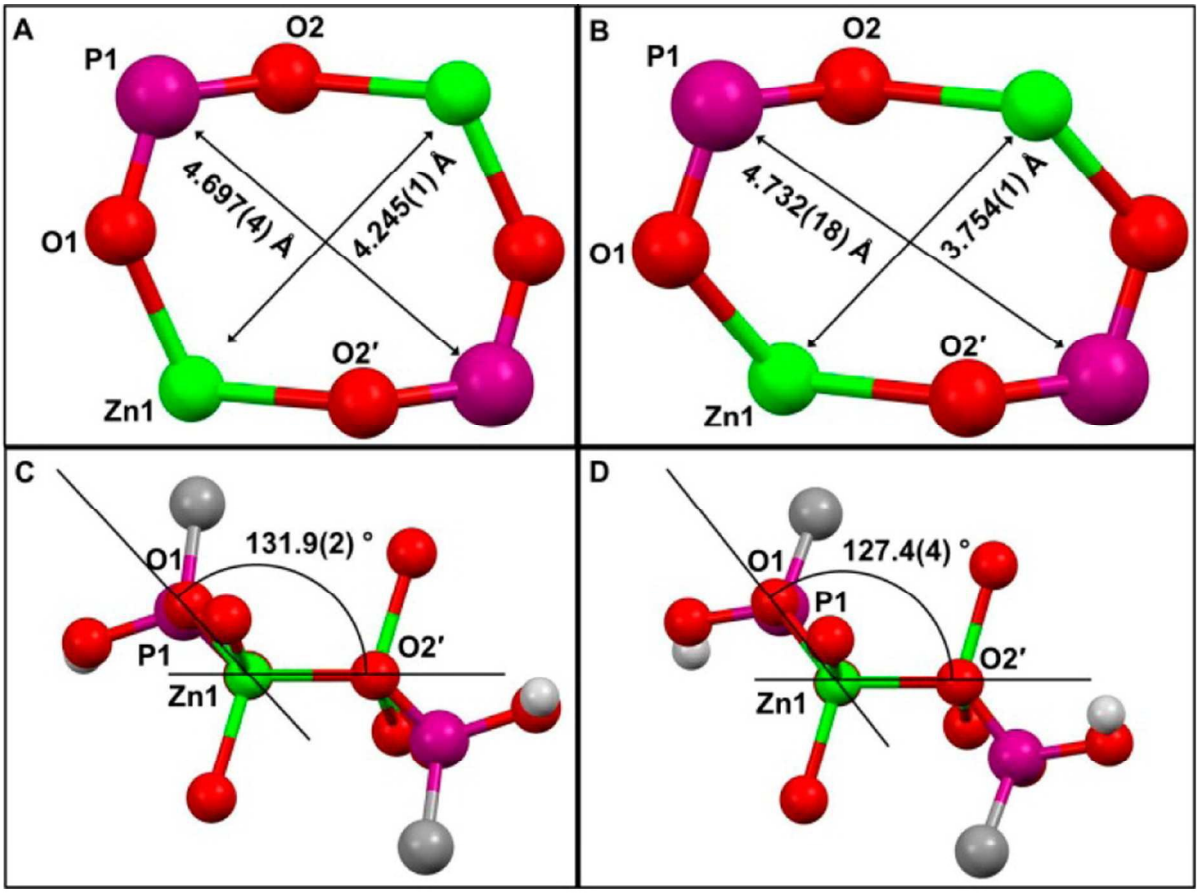


Figure 8. Representations of the 8-membered chain-link at ambient pressure (A, C) and 7.32(7) GPa (B, D) showing the ring (top) and the chair-like conformation (bottom). Solid black lines in the bottom represent calculated mean planes. The O1–Zn1–O2′ internal angle increases from 109.54(8) to 114.7(3)°. ′: −x+1,–y+1,–z+2. Used by permission of *J. Amer. Chem. Soc.* From ref. 13.

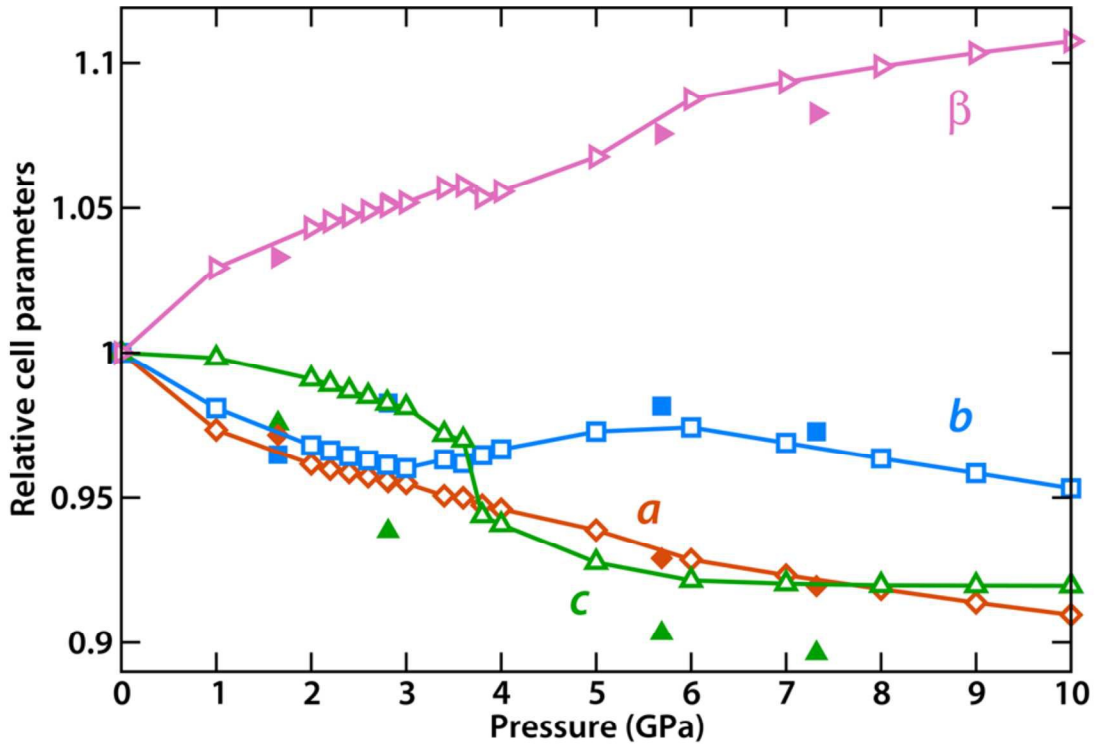


Figure 9. Evolution of the unit cell parameters of ZAG-4 as a function of pressure. Filled symbols: from in situ X-ray diffraction. Empty symbols: calculated by quantum mechanical enthalpy minimization. Reproduced from reference 14 with permission from *J. Amer. Chem. Soc.*

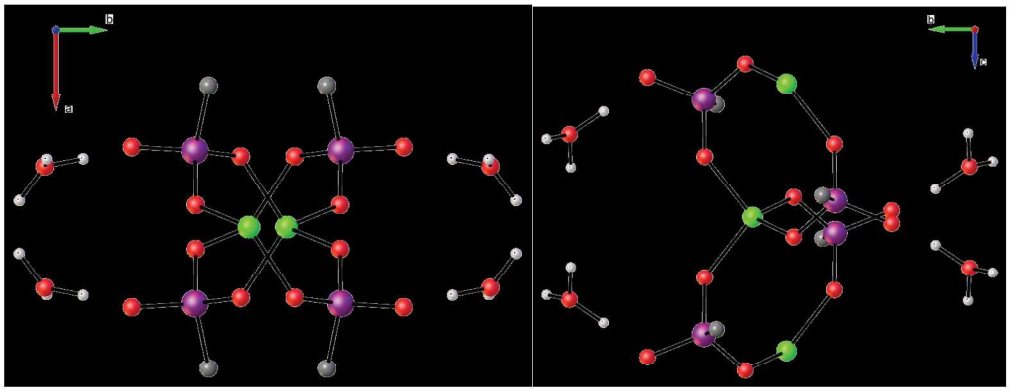

Figure 10. Visualization of part of the structure of ZAG-4 at 4 GPa, with the protonated water molecule and the nearby oxygen atom whose proton it abstracted. Left: view along the hinge of the wine rack (*b* axis); right: view in the perpendicular plain, with the phosphate-linked Zn chain clearly visible. In both cases, non-water hydrogen atoms were hidden for clarity's sake. Reproduced from ref. 14, S2 with permission from *J. Amer. Chem. Soc.*

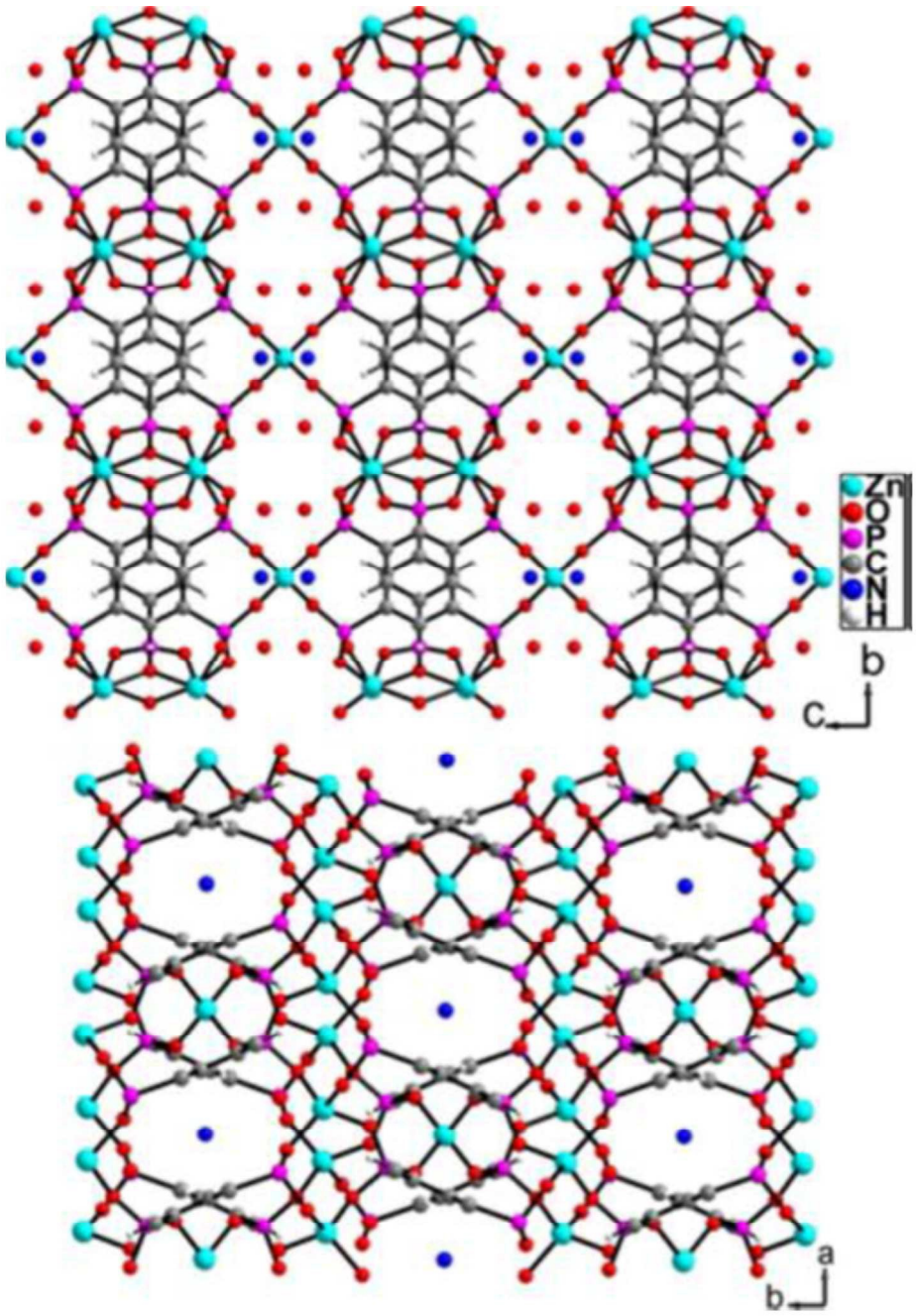


Figure 11. Views of the crystal structure along the *a* axis (top) and c axis (bottom) of ZnBP−NH4. Reproduced from ref. 28 with permission from *Crystal Growth and Design.*

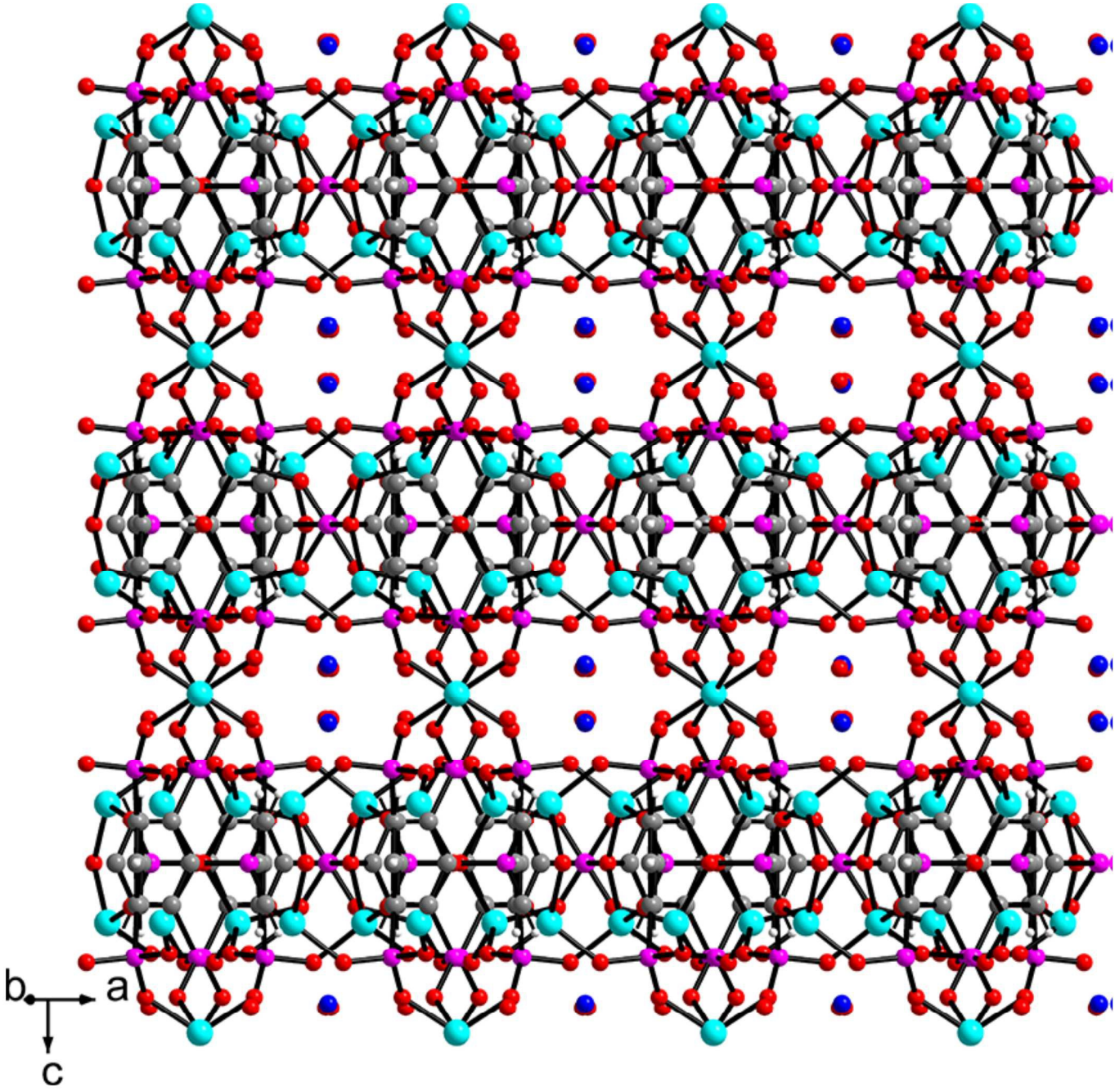


Figure 12. View of the smaller pores running along the [110] direction, which interconnects the larger pores. The organic–inorganic layers and the ZnO4 pillars can be clearly seen. The solvent molecules are disordered. Reproduced from ref. 28 with permission from *Crystal Growth and Design.*

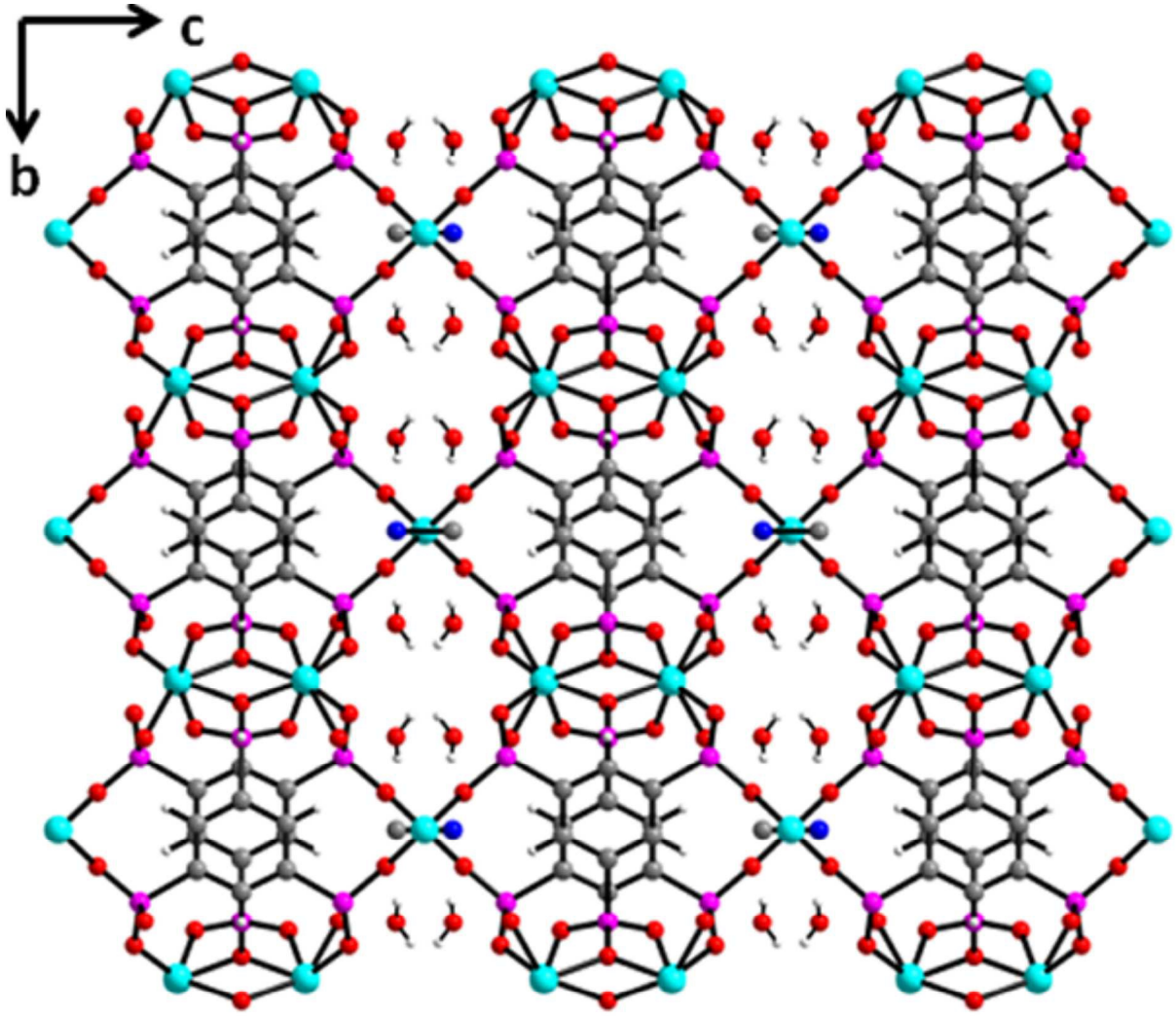


Figure 13. A view of the crystal structure along the a axis for ZnBP−$CH_3NH_3$. The $CH_3NH_3$ molecules are disordered. Note the similarity to the framework structure in figure 11. From ref. 28 with permission from *Crystal Growth and Design.*

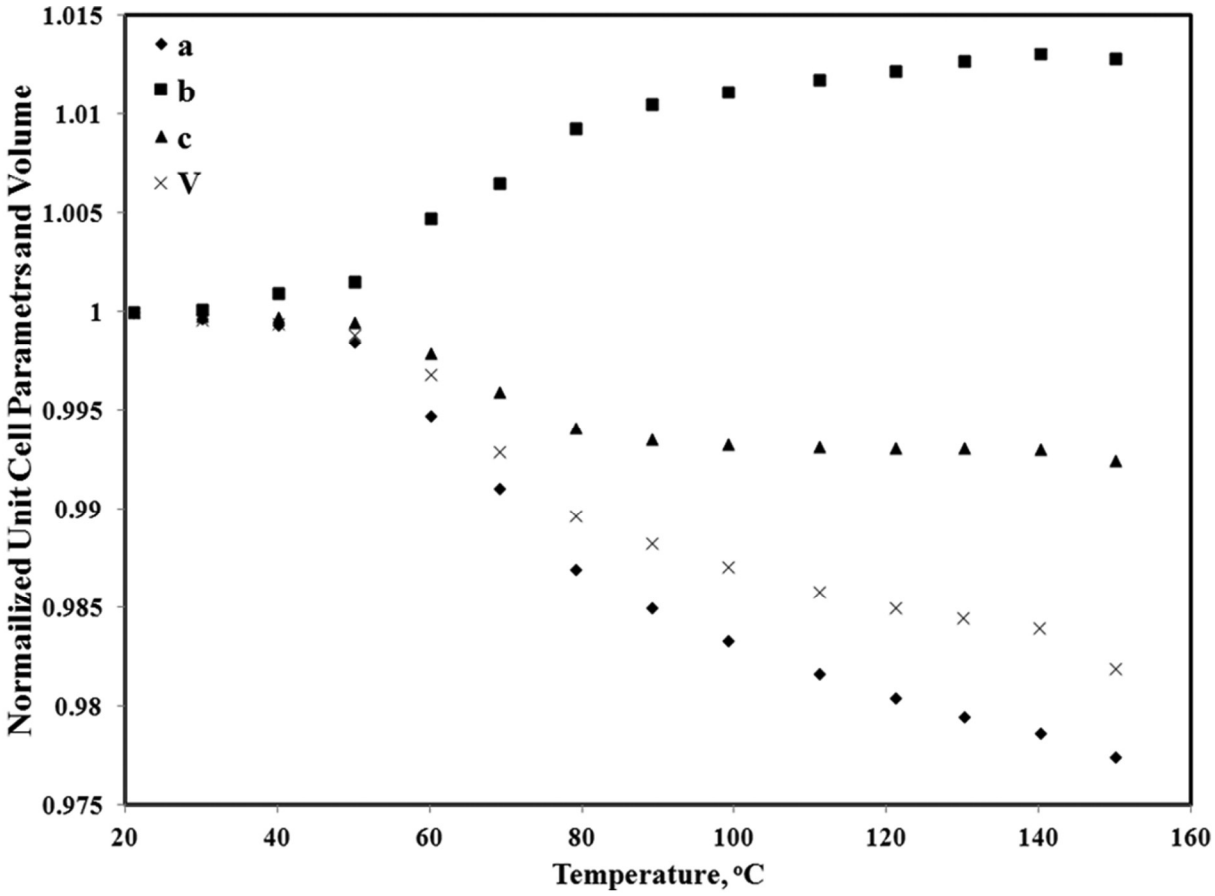


Figure 14. A plot showing the change in unit cell parameters and volume with increasing temperature. All data were normalized to the unit cell determined at room temperature. Reproduced with permission as for figure 13.

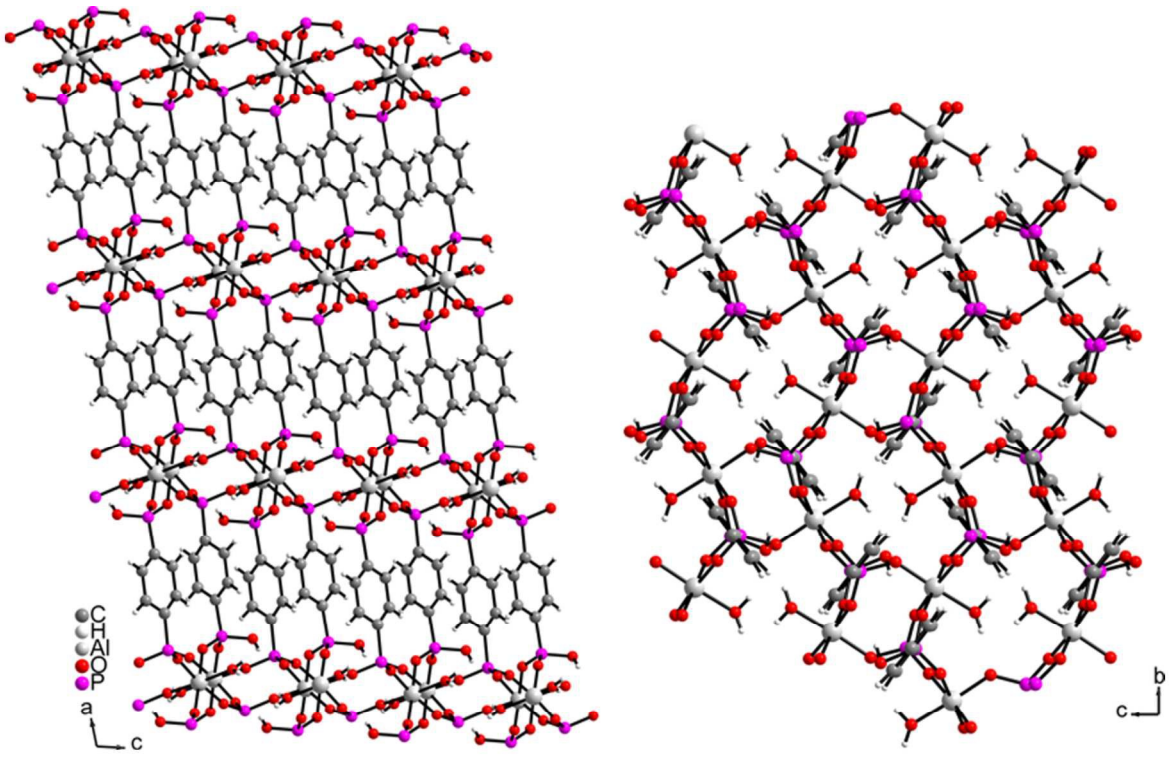


Figure 15. Two views of compound 1 showing how the pillars link the inorganic layer together (left) and the connectivity of the inorganic layers (right). From ref. 29 with permission from *Crystal Growth and Design*.

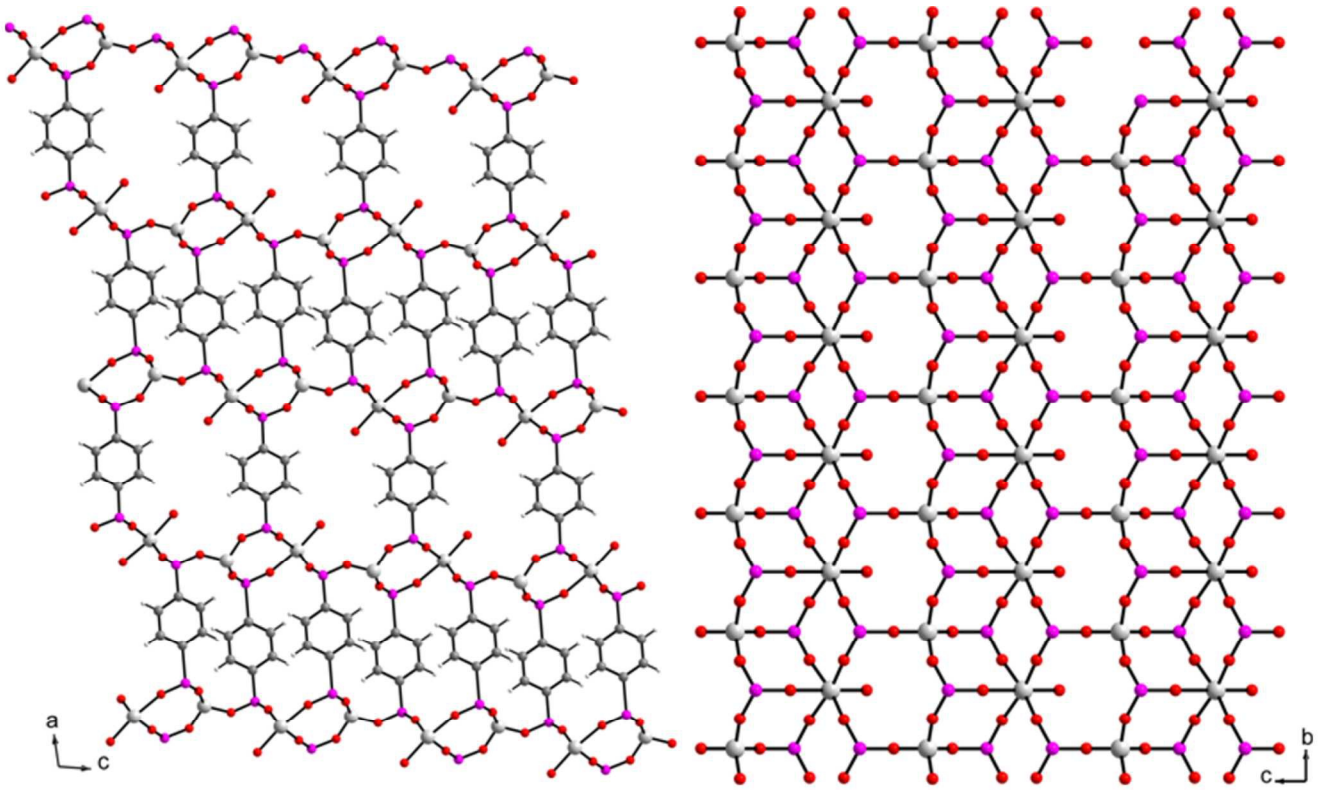


Figure 16. Crystal structure of compound 2 viewed down the b-axis (left) and the a-axis (right) showing the inorganic layer. From ref. 29 with permission from *Crystal Growth and Design.*

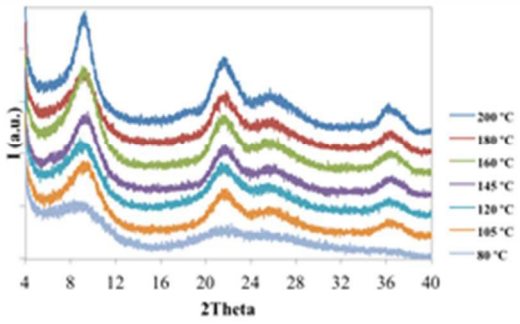


Figure 17. XRPD patterns of Sn-hybrid materials synthesized at 80-200 ºC.

Table 1. Crystallographic Data for ZAG-6*

| Sample | Ambient | 6.9 GPa |
|---|---|---|
| Chemical formula | $ZnP_2O_8C_6H_{18}$ | $ZnP_2O_8C_6H_{18}$ |
| Formula mass (g/mol) | 345.51 | 345.51 |
| Crystal system | Monoclinic | Monoclinic |
| Space group | C2/*c* | C2/*c* |
| λ (Å) | 0.6048 | 0.6702 |
| *a* (Å) | 23.180(5) | 19.782(4) |
| *b*(Å) | 8.2859(16) | 8.430(3) |
| *c* (Å) | 8.2008(16) | 7.7146(12) |
| *B* (deg.) | 120.3870(19) | 128.672(12) |
| *Z* | 4 | 4 |
| *V* (Å$^3$) | 1358.7(4) | 1004.4(4) |
| Temperature (K) | 296(2) | 296(2) |
| Density (g/cm$^3$) | 1.689 | 2.285 |
| Measured reflections | 9639 | 4317 |
| Unique reflections | 2697 | 587 |
| Parameters | 78 | 78 |
| Restraints | 0 | 0 |
| $R_{int}$ | 0.0715 | 0.0931 |
| $\vartheta$ range (deg.) | 4.989 – 28.213 | 3.458 – 25.412 |
| $R_1$, $wR_2$ all data | 0.0464, 0.1280 | 0.0606, 0.1517 |
| *S* (GoodF) all data | 0.993 | 1.114 |
| Max/min res. Dens. (e/Å$^3$) | 0.381/-0.473 | 1.054/-0.861 |

* All unit cells are reported as unconventional representations utilizing the transformation matrix 1020-1000-1. This was done to maintain the same orientation as in the ZAG-4 structure previously published.

Table 2. Crystallographic Parameters and Experimental Details for the Single Crystal Experiments.

| Crystal data | | | |
|---|---|---|---|
| | ZnBP-$NH_4$ (Phase Ia) | ZnBP-$NH_4$ (Phase Ib) | ZnBP-$CH_3NH_3$ |
| Chemical formula | $Zn_{2.5}(H)_{0.5}(C_6H_3O_9P_{3)}$ $(H_2O)_{1.9}(NH_4)_{0.5}$ | $Zn_{2.5}(H)_{0.4}(C_6H_3O_9P_3)$ $(H_2O)_{1.9}(NH_4)_{0.6}$ | $Zn_{2.5}(H)_{0.75}(C_6H_3O_9P_3)$ $(H_2O)_2(CH_3NH_3)_{0.25}$ |
| $M_r$ | 1036.91 | 1030.47 | 1027.85 |
| Crystal system, space group | Orthorhombic, *I bam* | Orthorhombic, *I bam* | Orthorhombic, *I bam* |
| Temperature (K) | 110 | 110 | 110 |
| *a*, *b*, *c*, (Å) | 8.472 (3), 16.208 (7), 19,816 (8) | 8.472 (3), 16.208 (7), 19,816 (8) | 8.430(5), 16.155 (12), 19,840 (11) |
| *V* (Å$^3$) | 2721.1 (19) | 2721.1 (19) | 2702 (3) |
| *Z* | 4 | 4 | 4 |
| μ (mm$^{-1}$) | 4.80 | 4.80 | 4.83 |
| Crystal size (mm) | 0.14 x 0.08 x 0.08 | 0.14 x 0.08 x 0.08 | 0.19 x 0.12 x 0.03 |
| $T_{min}$, $T_{max}$ | 0.555, 0.712 | 0.555, 0.712 | 0.460, 0.869 |
| No. of measured, Independent and Observed [$I > 2\,\sigma(I)$] reflections | 18603, 1746, 1330 | 18603, 1746, 1330 | 17603, 1550, 974 |
| $R_{int}$ | 0.073 | 0.073 | 0.204 |
| $(\sin\Theta/\lambda)_{max}$ (Å$^{-1}$) | 0.671 | 0.671 | 0.643 |
| $R[F^2>2\,\sigma(F^2)]$, $wR(F^2)$, $S$ | 0.034, 0.087, 1.03 | 0.036, 0.105, 1.02 | 0.061, 0.187, 1.11 |
| No. of reflections | 1746 | 1746 | 1550 |
| No. of parameters | 115 | 114 | 110 |
| No. of restraints | 0 | 0 | 12 |
| $\Delta P_{max}$,, $\Delta P_{min,}$ (e Å$^{-3}$) | 1.29, -1.09 | 1.88 -0.95 | 1.96, - 1.15 |

Taken from reference 28 Supplementary Data Table 1.

Table 3. Crystallographic Parameters and Experimental Details for the Rietveld Refinements

| Crystal data | | |
|---|---|---|
| | Phase II | Phase III |
| Chemical formula | $C_{12}H_6O_{18}P_6Zn_5{\cdot}4(O){\cdot}NH_4$ | $C_{12}H_6O_{18}P_6Zn_5{\cdot}NH_4$ |
| $M_r$ | 1028.9 | 968.9 |
| Crystal system, space group | Orthorhombic, *I bam* | Orthorhombic, *I bam* |
| Temperature (K) | 333 | 423 |
| *A, b, c*(Å) | 8.44254 (17),16.2851 (4),19.8132 (4) | 8.295735 (18), 16.4162 (4), 19.7053 (5) |
| *V*(Å$^3$) | 2724.06 (10) | 2683.55 (11) |
| *z* | 4 | 4 |
| Radiation type | Synchrotron,λ=0.6124 Å | Synchrotron,λ=0.6124 Å |
| Diffractometer | Diffractometer at APS 1-BM-C | Diffractometer at APS 1-BM-C |
| Specimen mounting | Kapton capillary, 0.9mm diameter | Kapton capillary, 0.9mm diameter |
| Data collection mode | Fixed | Fixed |
| Scan method | Stationary detector | Stationary detector |
| 2Θvalues ($^o$) | $2\Theta_{min}$=3.269<br>$2\Theta_{max}$=24.994<br>$2\Theta_{step}$=0.013 | $2\Theta_{min}$=3.269<br>$2\Theta_{max}$=24.994<br>$2\Theta_{step}$=0.013 |
| *R*factors | $R_p$=0.061,$R_{wp}$=0.085,$R_{exp}$=0.048<br>$R(F)$ = 0.034,,$\chi^2$= 3.168 | $R_p$=0.050, $R_{wp}$=0.069, $R_{exp}$=0.031,<br>$R(F)$ = 0.047,$\chi^2$= 4.410 |
| No. of data points | 1739 | 1763 |
| No. of parameters | 72 | 75 |
| No. of restraints | 11 | 11 |
| H-atom treatment | H-atom parameters constrained | H-atom parameters constrained |

Table 4. Crystallographic Parameters and Experimental Details for the Rietveld Refinements

| Crystal data | | |
|---|---|---|
| | Phase II | Phase III |
| Chemical formula | $C_{12}H_6O_{18}P_6Zn_5{\cdot}4(O){\cdot}NH_4$ | $C_{12}H_6O_{18}P_6Zn_5{\cdot}NH_4$ |
| $M_r$ | 1028.9 | 968.9 |
| Crystal system, space group | Orthorhombic, *I bam* | Orthorhombic, *I bam* |
| Temperature (K) | 333 | 423 |
| *A, b, c*(Å) | 8.44254 (17),16.2851 (4),19.8132 (4) | 8.295735 (18), 16.4162 (4), 19.7053 (5) |
| $V$(Å$^3$) | 2724.06 (10) | 2683.55 (11) |
| *z* | 4 | 4 |
| Radiation type | Synchrotron,λ=0.6124 Å | Synchrotron,λ=0.6124 Å |
| Diffractometer | Diffractometer at APS 1-BM-C | Diffractometer at APS 1-BM-C |
| Specimen mounting | Kapton capillary, 0.9mm diameter | Kapton capillary, 0.9mm diameter |
| Data collection mode | Fixed | Fixed |
| Scan method | Stationary detector | Stationary detector |
| 2Θvalues (°) | $2\Theta_{min}$=3.269<br>$2\Theta_{max}$=24.994<br>$2\Theta_{step}$=0.013 | $2\Theta_{min}$=3.269<br>$2\Theta_{max}$=24.994<br>$2\Theta_{step}$=0.013 |
| *R*factors | $R_p$=0.061,$R_{wp}$=0.085,$R_{exp}$=0.048<br>$R(F)$ = 0.034,,$\chi^2$= 3.168 | $R_p$=0.050, $R_{wp}$=0.069, $R_{exp}$=0.031,<br>$R(F)$ = 0.047,$\chi^2$= 4.410 |
| No. of data points | 1739 | 1763 |
| No. of parameters | 72 | 75 |
| No. of restraints | 11 | 11 |
| H-atom treatment | H-atom parameters constrained | H-atom parameters constrained |